

# **Observing the Sun from start to finish: The Tunable magnetograph's design, calibration, data reduction and scientific exploitation.**

PhD dissertation by

**Pablo Santamarina Guerrero**

Instituto de Astrofísica de Andalucía (IAA-CSIC)

Programa de Doctorado en Física y Matemáticas (FisyMat)  
Universidad de Granada

A thesis submitted in fulfillment  
of the requirements of the degree of  
Doctor of Philosophy

September 19, 2024

PhD thesis supervised by

**Dr. David Orozco Suárez**

**Dr. Julián Blanco Rodríguez**



INSTITUTO DE  
ASTROFÍSICA DE  
ANDALUCÍA



EXCELENCIA  
SEVERO  
OCHOA



**UNIVERSIDAD  
DE GRANADA**



# CONTENTS

<b>1</b>	<b>Introduction</b>	<b>1</b>
1.1	Background . . . . .	1
1.2	Motivation of our work . . . . .	2
1.3	Introduction . . . . .	4
1.4	A brief introduction to spectropolarimeters. . . . .	5
1.4.1	Imaging and optical quality. . . . .	5
1.4.2	Spectroscopy . . . . .	10
1.4.3	Polarimetry . . . . .	12
1.4.4	Imaging . . . . .	13
1.4.5	What do spectrpolarimeters tell us about the Sun? . . . . .	14
<b>2</b>	<b>TuMag’s design and calibration.</b>	<b>17</b>
2.1	Sunrise III . . . . .	18
2.2	The Tunable magnetograph: TuMag . . . . .	18
2.3	TuMag’s design and light path. . . . .	18
2.4	Instrument performance and verification. . . . .	20
2.4.1	Imaging performance. . . . .	20
2.4.2	Verification . . . . .	24
2.4.3	Spectral performance. . . . .	24
<b>3</b>	<b>TuMag’s pipeline and data.</b>	<b>27</b>
3.1	TuMag’s observing modes . . . . .	27
3.1.1	Calibration modes . . . . .	28
3.2	Pipeline . . . . .	28
3.2.1	Darks and flat fields . . . . .	28
3.2.2	Blueshift . . . . .	28
3.2.3	Demodulation and dual beam . . . . .	28
3.2.4	Cross Talk . . . . .	28



# CHAPTER 1

---

## INTRODUCTION

### 1.1 Background

In June 2009, the first Sunrise observatory (Barthol et al., 2011) was launched from Kiruna, Sweden, aboard a stratospheric balloon. Equipped with a 1-m aperture telescope, a multi-wavelength UV filter imager, and IMaX, a Fabry-Pérot-based magnetograph, Sunrise was the most complex payload carried by a solar stratospheric balloon to date. Aimed at studying the magnetic fields of the Sun and the dynamics of solar plasma convective flows, the mission was an outstanding success. It resulted in the publication of over a hundred peer-reviewed scientific articles in numerous high-impact journals, including *Astronomy and Astrophysics* (A&A), *The Astrophysical Journal* (APJ), and *Solar Physics*, among others.

Following the success of its inaugural flight, Sunrise embarked on a second journey (Solanki et al., 2017) on June 13, 2013. The primary objective of this subsequent flight was to investigate the active regions of the Sun, as it remained completely *quiet* throughout the entirety of the initial flight. Despite minimal alterations to the instrumentation aboard the observatory, the variance in solar activity during this second flight yielded fresh perspectives and valuable data, ultimately securing the mission success, despite encountering some technical challenges.

Given the success of the first two flights, a third iteration of the Sunrise mission was planned, featuring an updated design. For this third edition, the telescope was equipped with three post-focal instruments: SUSI, a UV spectrograph; SCIP, an infrared spectrograph; and TuMag, the evolution of the IMaX magnetograph. Sunrise III was initially scheduled to fly during the summer of 2020 but was postponed to 2022.

The third launch of Sunrise plays a crucial role in this dissertation. This thesis, initiated in 2020, was centered on the development of the data reduction pipeline for the TuMag instrument, which was entirely developed by the Spanish solar physics consortium. According to the original plan, the first half of the thesis was dedicated to the calibration of the instrument and the preparation of the data pipeline. This way, once the mission was launched, the second half of the thesis could focus on the correction and scientific analysis of the data produced during this third flight. However, this plan (and thus the scope of the thesis) encountered a setback on July 10, 2022, when the third flight of the Sunrise observatory had to be aborted just a few hours after the launch due to a mechanical failure during

the ascent phase.

The observatory was recovered days later after a brief stay in the Scandinavian Alps. Both the telescope and the instruments were found to be in good condition, allowing for the recovery of the observatory and providing hope for a second attempt. However, the process of retrieving the instruments, disassembling, calibrating, and verifying their condition before relaunching the mission is lengthy, and it was not until this year, 2024, that a second attempt became feasible.

In the absence of data produced by Sunrise to process, analyze, and exploit, the scientific work conducted within the framework of this thesis has been compelled to slightly shift its focus. Over these years, we have focused on delving deeper into image correction techniques for data obtained from Fabry-Pérot interferometers, such as TuMag and IMaX. As well as conducting several studies using data products from other instruments, such as the Polarimetric and Helioseismic Imager aboard Solar Orbiter (SO/PHI) and HMI.

It wasn't until the 10<sup>th</sup> of July of 2024 that Sunrise III got its second chance to fly, and this time, the opportunity was not wasted. After a very successful flight that lasted 6 days, the observatory landed in the northern region of Canada on the XX of July. Figure XX shows the trajectory our favourite solar observatory followed over these days. The recovery process started immediately after landing, and we were able to lay hands on the data for the first time on September 2024.

In the following chapters, we will present the work undertaken during the calibration and commissioning of TuMag, conducted in 2021, 2022, and 2024. Additionally, the research carried out between the first and second flights of Sunrise III, which has resulted in the publication of two articles as the main author — one published in APJ and the other in A&A — will also be detailed in this manuscript, as well as other studies that have not yet been published in any scientific journal.

## 1.2 Motivation of our work

In experimental sciences, there is a very strong relation between technological and scientific advances due to the simple fact that we cannot draw conclusions from what we cannot see. We believe it is important for experimental scientists, and more specifically, for observational astronomers, to know the limitations and capabilities and understand the functioning of the instruments we use.

This philosophy is one of the pillars of this thesis, which covers topics ranging from the design and calibration of scientific instruments to the exploitation of the data they produce. With this thesis, we aim to provide a broad, yet detailed, view of the various stages of a scientific mission, from its conception and objectives through its design and calibration, data reduction and preparation for scientific exploitation, and finally, the studies and conclusions derived from it.

In particular, we will detail this process within the framework of solar physics through the development of TuMag, the magnetograph aboard Sunrise III. We will present the scientific objectives of the mission and attempt to link the design concepts with the scientific

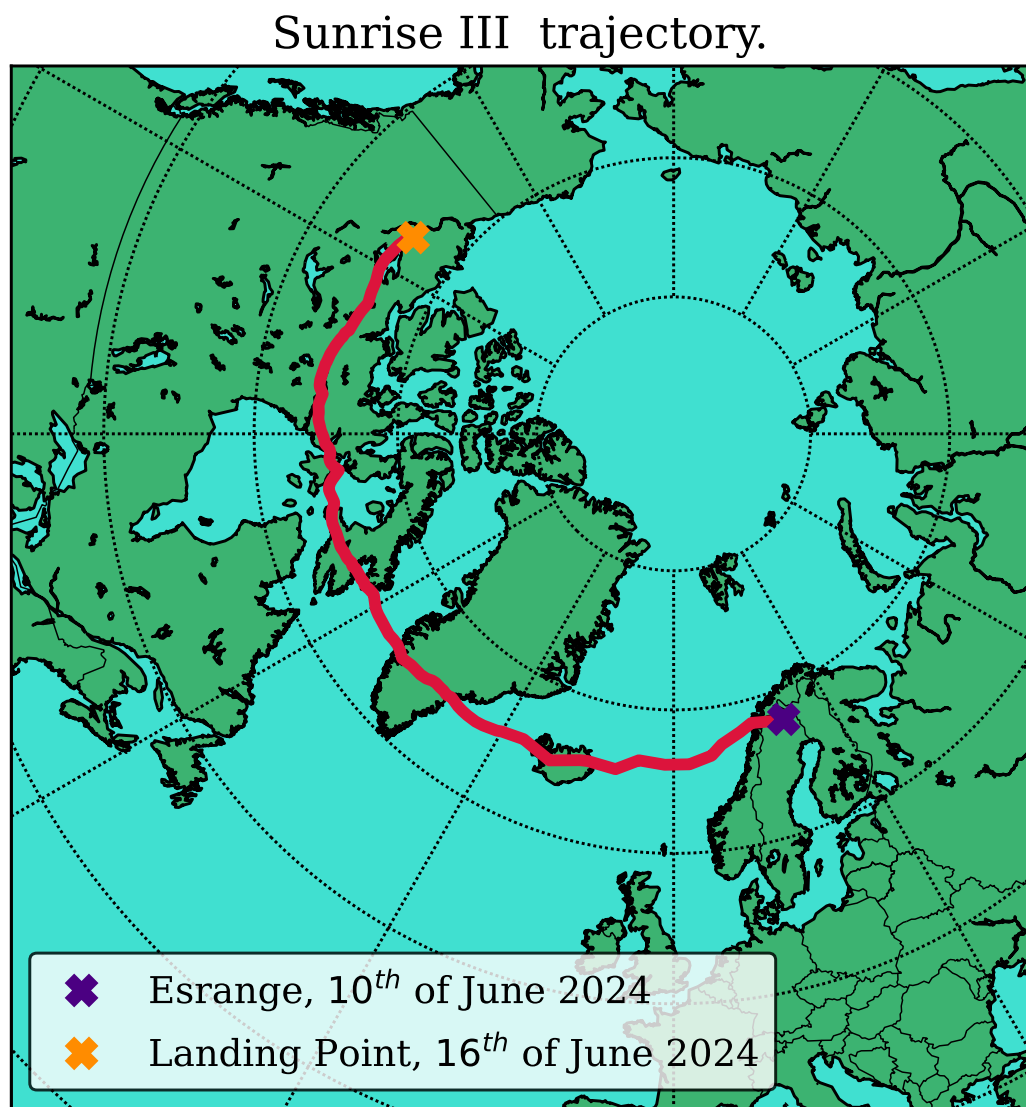


Figure 1.1 Sunrise III trajectory.

questions we aim to answer. We will address the challenges encountered in data correction due to the technical or instrumental limitations, a subject of ongoing debate within the community and of current relevance. And finally, we also aim to offer a brief dip into the scientific exploitation that can be carried out with the final data product.

With this thesis we aim to clarify the following points:

- ✿ Scientific objectives of TuMag.
- ✿ Instrumental ways of achieving the scientific purposes
- ✿ Open problems for data reduction. Flat-fields, etalon effects in the data.
- ✿ Offering an example of data exploitation with a study case. Persistent Homology.

## 1.3 Introduction

Astronomy is one of the broadest fields of knowledge. It studies everything from the smallest astronomical objects, such as the small asteroids that inhabit our solar system, to the global structure and evolution of the universe, including the study of planetary systems, stars, black holes and the galaxies in which they are found. However, despite the diversity of disciplines—ranging from stellar astronomy, radio astronomy, and cosmology, to extragalactic astronomy, astrobiology, and solar physics—they all share a common tool for studying the cosmos: light. Since the very beginning of astronomy, the astronomer’s work has been to learn how to modify and measure the properties of the photons that reach us in order to infer the characteristics of the observed object. Although recent advancements have provided astronomers with new lenses to *see* the cosmos, like gravitational waves (**REFERENCIA**) or neutrinos (**REFERENCIA**), among others, light remains as our main resource. Our understanding of the cosmos has always gone hand-in-hand with our ability to design and develop new (or more efficient) and clever ways to dissect the light, spanning from the first solar clocks, passing through Newton’s first telescope to the modern-day spaceborne telescopes like the Hubble, James Webb or Solar Orbiter.

Solar physics is no different from other astronomical disciplines in this regard. Our main tool to *see* the Sun is through light. Contrary to what one may think, solar physicists are as photon-starved as any other astronomer. Even though our star is closer and (apparently) brighter than any other astronomical object, our requirements regarding resolution and sensitivity are so high that we are as dependent on extremely optimized instrumentation as any other discipline. Thus, the development of instrumentation employing state-of-the-art technology and techniques plays an important role in modern solar physics.

## 1.4 A brief introduction to spectropolarimeters.

Spectropolarimeters, as suggested by the name, are devices that measure the spectral and polarimetric properties of light, or in other words, that measure the polarization state of light as a function of wavelength. Their use is widely extended in astrophysics due to the huge amount of information about the light source we can infer from these properties.

In solar physics, it is common to encounter two distinct types of spectropolarimeters, distinguished by their approach to spectroscopy: slit-based spectrographs, such as SUSI and SCIP, and narrow-band tunable filtergraphs, like TuMag. The latter preserve spatial resolution by capturing two-dimensional images of the solar scene at the expense of sacrificing spectral resolution. Conversely, slit-based spectrographs provide excellent spectral resolution but have a limited spatial resolution.

Regardless of how spectroscopy is carried out, spectropolarimeters must be able to measure the polarization state of light. That is, they must be capable of determining the Stokes parameters of the incident light. These four parameters, usually grouped in a pseudo-vector:  $[I, Q, U, V]$ , were defined by Stokes in Stokes (1851) as a mathematical formalism to completely define the polarization state of light. The first parameter,  $I$ , represents the total intensity;  $Q$  and  $U$  provide information about the intensity of linearly-polarized light, at  $0^\circ$  and  $90^\circ$ , respectively; and lastly,  $V$ , accounts for the intensity of circularly polarized light.

Excellent polarimetric sensitivity and spectral resolution are wasted if the optical capabilities of the instrument are not up to par. The design of these instruments must achieve diffraction-limited imaging, with a signal-to-noise ratio ensuring a polarimetric sensitivity of 1000 (typically), and the best spatial resolution the telescope allows, all without sacrificing spectral resolution and accomplishing this in the shortest possible time.

When designing the instrument, one must balance these three properties: spectral, optical, and polarimetric capabilities, trying to improve the performance in all of them without sacrificing too much. In the following sections, we will delve into each of these aspects in more detail.

### 1.4.1 Imaging and optical quality.

Filtergraphs are, first and foremost, imagers. The high-resolution imaging that filtergraph instruments are capable of is one of the pivotal reasons for their extended use. The ability to capture a two-dimensional scene of the solar surface makes them ideal for studying solar plasma structures, which require resolutions close to 100 km on the solar photosphere. These instruments must be able to ensure an image quality and resolving power enough to measure these structures. For this reason, we will begin our description of the filtergraphs with a brief explanation of image formation and image quality assessment.

Let us assume that the extended source we are observing has an intensity distribution in the image plane given by  $O(\xi_0, \eta_0)$ . Then, if we assume a linear optical system and incoherent illumination, the intensity distribution measured at a point  $\xi, \eta$  of the image is given by :

$$I_j(\xi, \eta; \lambda_s) = \iint O(\xi_0, \eta_0) S(\xi_0, \eta_0; \xi, \eta; ) d\xi_0 d\eta_0, \quad (1.1)$$

where  $S(\xi_0, \eta_0; \xi, \eta; )$  represents the imaging response of the instrument, also referred to as the Point Spread Function (PSF). The PSF describes the normalized intensity distribution in the image plane when observing a point source, which, due to diffraction and inherent imperfections in any imaging system, cannot be imaged as an ideal point.

The PSF is crucial in the assessment of image quality and resolving power of an instrument since it defines how fine detail will be imaged into the detector. One particularly relevant metric for image quality assessment that can be derived from the PSF is the optical transfer function (OTF), which is the Fourier transform of the PSF (Vargas Dominguez, 2009a).

$$OTF(v) = \mathcal{F} [S(\xi_0, \eta_0; \xi, \eta; )], \quad (1.2)$$

where the operator  $\mathcal{F}$  is the Fourier transform, and  $v$  the spatial frequencies.

The OTF describes how different spatial frequencies are transferred from the object to the image, thus characterizing the system's ability to resolve fine details. However, since imaging systems measure intensities, we are primarily concerned with how the intensity pattern of an object is transferred to the image. A key metric for quantifying this transfer is modulation, or contrast, which is defined as the ratio between the peaks and valleys of intensity at a given spatial frequency:

$$M_v = \frac{I_{max}^v - I_{min}^v}{I_{max}^v + I_{min}^v}. \quad (1.3)$$

The function that encodes the dependency of the modulation with spatial frequencies is called the modulation transfer function (MTF), ands strictly related to the OTF as the ratio of the modulation of the object  $MTF_{obj}$  and that of the image  $MTF_{im}$ can be computed from the magnude of the OTF (Gaskill, 1978):

$$MTF = \frac{MTF_{im}(v)}{MTF_{obj}(v)} = |OTF(v)|. \quad (1.4)$$

From this definition, it is evident that a perfect optical system would have an  $MTF = 1$  at all spatial frequencies, meaning that all details are perfectly transferred from the object to the image. However, real optical systems exhibit a decrease in MTF as spatial frequency increases. In practice, the resolution of an optical system can, and is often defined as the spatial frequency at which both the MTF and, consequently, the OTF reach zero (Tyson, 2000). This threshold frequency marks the limit beyond which the system can no longer resolve finer details.

Another key concept for assessing the imaging performance is the phase error or wavefront. The wavefront of an optical system is defined as the deviation in phase at any point within the image from that of an ideal spherical wavefront (Snyder, 1975). Such deviations arise from various optical imperfections within the imaging system, and their impact on

image quality depends on the specific nature of the aberration. For instance, imperfections in mirror shape or lens configuration can result in spherical aberrations, leading to a broadening of the point spread function (PSF) and a subsequent reduction in resolution. Other common aberrations include astigmatism, where the focal point varies along different axes, producing distorted images, and comatic aberrations (coma), which can occur due to misalignment of optical elements and manifest as tail-like distortions in the images of point sources.

It is common to see requirements or assessment of the optical quality in terms of the root mean square (rms) of the variance of the wavefront,  $\Delta\phi(\xi, \eta)$ , usually referred to as the wavefront error (rms WFE) or simply WFE:

$$WFE = \sqrt{\frac{1}{A} \int_A (\Delta\phi(\xi, \eta))^2 d\xi d\eta}, \quad (1.5)$$

where  $A$  is the area of the aperture.

This value, essentially the standard deviation of the wavefront across the FoV, is closely tied to beam propagation quality. In fact, it can be demonstrated that the wavefront variance can be derived from the Strehl ratio, or conversely, the Strehl ratio can be computed from the wavefront error. The Strehl ratio is defined as the ratio of the peak intensity of a point source in an aberrated system to that of an ideal system operating at the diffraction limit. It is one of the most widely used metrics for assessing the optical quality of a system, ranging from 1, for a perfect, unaberrated system, to 0. For small aberrations, the Strehl ratio (SR) and WFE are related by the following expression (Snyder, 1975):

$$SR \simeq \exp \left[ - \left( \frac{2\pi WFE}{\lambda} \right)^2 \right]. \quad (1.6)$$

Although the Strehl ratio and rms WFE provide a concise measure of the optical quality of a system, the WFE contains additional information that can further elucidate imaging performance. Rather than relying solely on a single averaged value (such as the standard deviation), the wavefront can be represented as a two-dimensional map projected onto a plane normal to the light path, typically the image plane. To carry out such a representation analytically, it is essential to select an appropriate mathematical framework. Given the widespread use of circular apertures in telescopes, mirrors, lenses, and other optical components, it is advantageous to approach the problem using polar coordinates,  $\rho$  and  $\theta$ , and in particular, to employ an orthonormal basis for the interpretability of the results. Among the multiple (infinite) sets of polynomials that fulfill these requirements, the Zernike polynomials (Zernike, 1934) offer some distinct advantages. The Zernike polynomials are a sequence of polynomials that compose an orthonormal basis over a unit circle. Given an arbitrary wavefront,  $(W(\rho, \theta))$ , the expansion in terms of the Zernike polynomials can be expressed as:

$$W(\rho, \theta) = \sum_{n,m} C_n^m Z_n^m(\rho, \theta), \quad (1.7)$$

where  $Z_n^m$  are the Zernike polynomials,  $C_n^m$  are the amplitudes of the coefficients in the expansion and  $n$  and  $m$  are the radial order and angular frequency, respectively. The Zernike polynomials can be obtained from:

$$\left. \begin{aligned} Z_n^m(\rho, \theta) &= R_n^m(\rho) \cos(m\theta), \text{ for } m \geq 0, \\ Z_n^{-m}(\rho, \theta) &= R_n^m(\rho) \sin(m\theta), \text{ for } m < 0, \end{aligned} \right\} \quad (1.8)$$

where  $R_n^m(\rho)$  are the radial functions given by:

$$R_n^m(\rho) = \sum_{l=0}^{(n-m)/2} \frac{(-1)^l (n-l)!}{l! \left[ \frac{1}{2}(n+m)-l \right]! \left[ \frac{1}{2}(n-m)l \right]!} \rho^{n-2l}. \quad (1.9)$$

This representation of the wavefront is particularly valuable because each mode, defined by a specific pair of  $n$  and  $m$  values, corresponds to a distinct aberration in the wavefront, with the associated coefficient representing the rms WFE for that specific aberration. Furthermore, the orthogonality of the Zernike basis ensures that adding additional terms to the expansion does not influence the values of previously calculated coefficients. In other words, the Zernike polynomial expansion enables the wavefront to be expressed as the sum of individual aberrations, providing a clear decomposition of the wavefront errors.

Figure 1.2 presents an example of a simulated wavefront, including a two-dimensional cross-section and the individual Zernike components of the simulation. The simulation incorporates only the first ten Zernike polynomials, corresponding to polynomials with  $n \leq 3$ , which account for aberrations such as defocus, astigmatism, coma, and trefoil, among others. For a comprehensive overview of the Zernike expansion in wavefront characterization, we direct the reader to Lakshminarayanan & Fleck (2011).

Although properties such as the PSF and WFE provide us with a lot of information to evaluate the instruments performance they are not known a priori. Instruments need to be equipped with means to measure these quantities in order to assess the performance and correct for any defects. The strategy to follow depends on the properties of the instrument, for instance, onground instruments may be equipped with adaptive optics technology where the wavefront is directly measured and corrected for in real time. (REFERENCIAS). However, this approach is not feasible in all instruments, such as space-born instruments, for example, thus, other methods are required. One approach of special relevance for this purpose is the phase diversity technique.

The phase diversity algorithm (Childlaw et al., 1979) is a method to infer the aberrations present in an optical system by obtaining, at least, two simultaneous, or quasi-simultaneous, images of the same object introducing an additional and known aberration to one of the images.

The algorithm works by minimizing a cost function that depends on the OTF of the system which can be parametrized by the Zernike expansion (Paxman et al., 1992):

$$\mathcal{L}(C) = \sum_k \frac{|I_1(u)S_2(u, C) - I_2(u)S_1(u, C)|^2}{|S_1(u, C)|^2 + |S_2(u, C)|^2}, \quad (1.10)$$

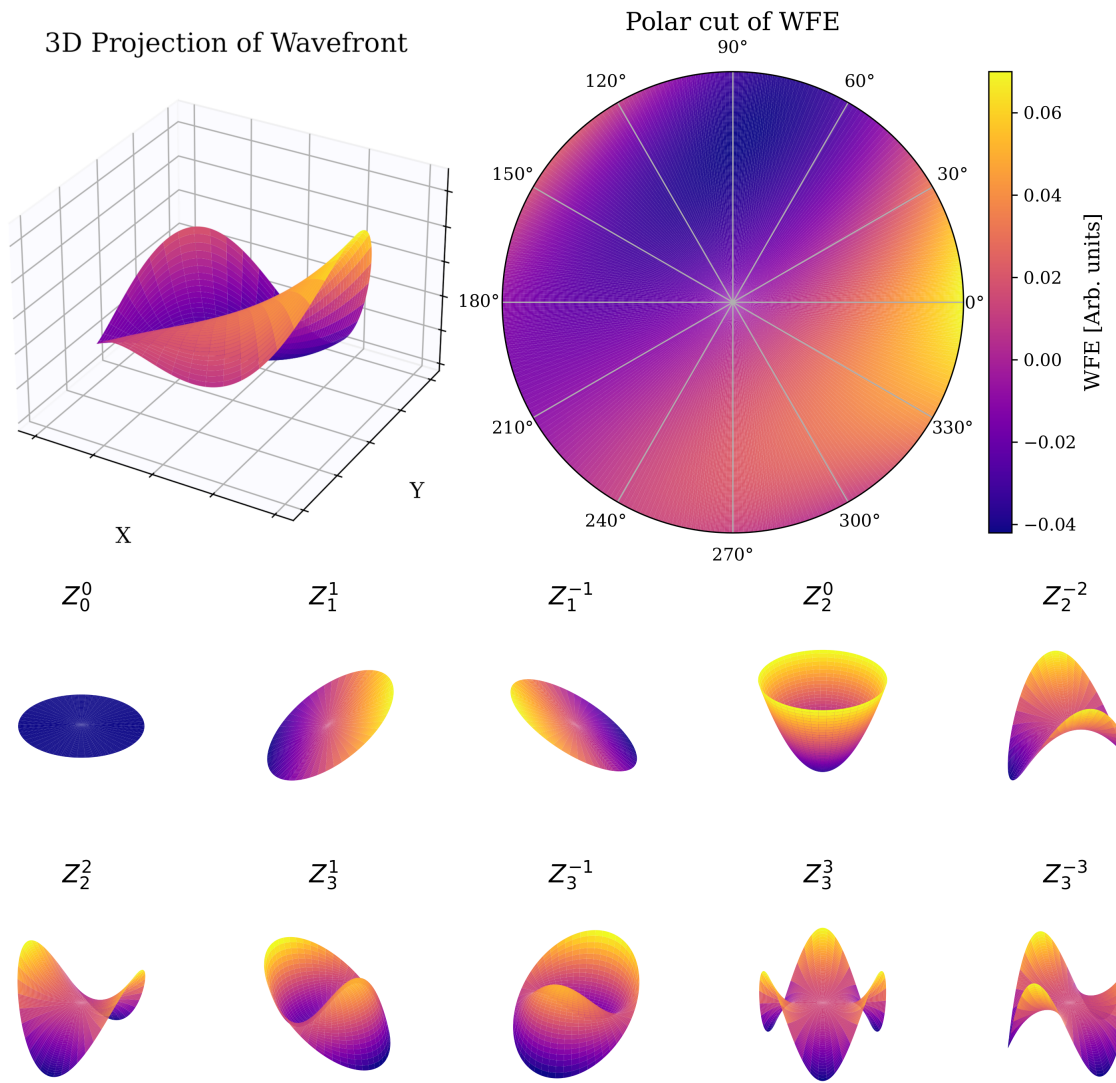


Figure 1.2 Simulation of a wavefront employing all Zernikes with  $n \leq 3$ . The top left panel shows the 3-dimensional representation of the wavefront and the top right panel shows a cut in a plane normal to the direction of travel. The bottom two rows show the shape of the individual Zernike polynomials included in the simulation.

where  $k$  represents the pairs of aberrated (subindex 1) and unaberrated (subindex 2) images,  $u$  is the frequency vector in the Fourier domain,  $I$  stands for the intensity distributions,  $S$  for the system's OTF expressed in terms of a Zernike expansion with coefficients  $C$ .

By finding the coefficients of the zernike expansion that minimize  $\mathcal{L}$ , we are able to characterize the wavefront and identify the aberrations present in the optical system. Thus, determining the OTF, and consequently the PSF.

We are interested in determining the wavefront and OTF not only as a quality indicator of the instrument but also because it allows us to restore the image and remove the effects that the aberrations introduce into the image.

The process of removing the effects of the aberrations consists on extracting the effects of the PSF into the final intensity, or in other words, we need to *deconvolve* the PSF from the image. Coming back to equation (1.1), we can simplify the integrals to a convolution operator in the Fourier domain assuming an spatial invariance of the PSF. In that case, the observed intensity can be expressed by:

$$I(\xi, \eta) = O(\xi, \eta) * S(\xi, \eta) + v(\xi, \eta) \quad (1.11)$$

where we added a term accounting for the noise present in real measurements  $v(\xi, \eta)$ .

The determination of  $O(\xi, \eta)$  is easier to compute in the fourier domain, since the convolution operator can be expressed as the product of the corresponding fourier transformation. Taking this into account and doing a simple rearrangement of equation (1.11), we can determine the object through:

FILTRO OPTIMO?

RESUMEN?

### 1.4.2 Spectroscopy

Narrow-band tunable spectrographs play a significant role in this thesis. They will be extensively discussed in this chapter, particularly in relation to the design and calibration of TuMag, and again in Chapters 3 and ?? when addressing TuMag's pipeline and the correction of data produced by these instruments. Therefore, for the sake of simplicity, we will focus exclusively on this type of spectrographs from this point onward.

**CAMBIAR ESTO.**

Fabry-Pérot Interferometers (FPIs), also known as etalons (used interchangeably), represent one of the most prevalent forms of narrow-band tunable spectrographs. Composed by a resonant optical cavity formed by two distinct optical media, these devices allow only the passage of light with wavelengths corresponding to constructive interference within the cavity.

The transmission profile of an etalon, being produced by an interference phenomenon, is characterized by a series of narrow and periodic transmission peaks. The wavelengths at which this resonance peaks are located, their width, and their separation are determined solely by the physical properties of the etalon. In fact, it is not difficult to demonstrate (Bailén et al., 2019) that a resonant cavity produces a periodic transmission profile, with

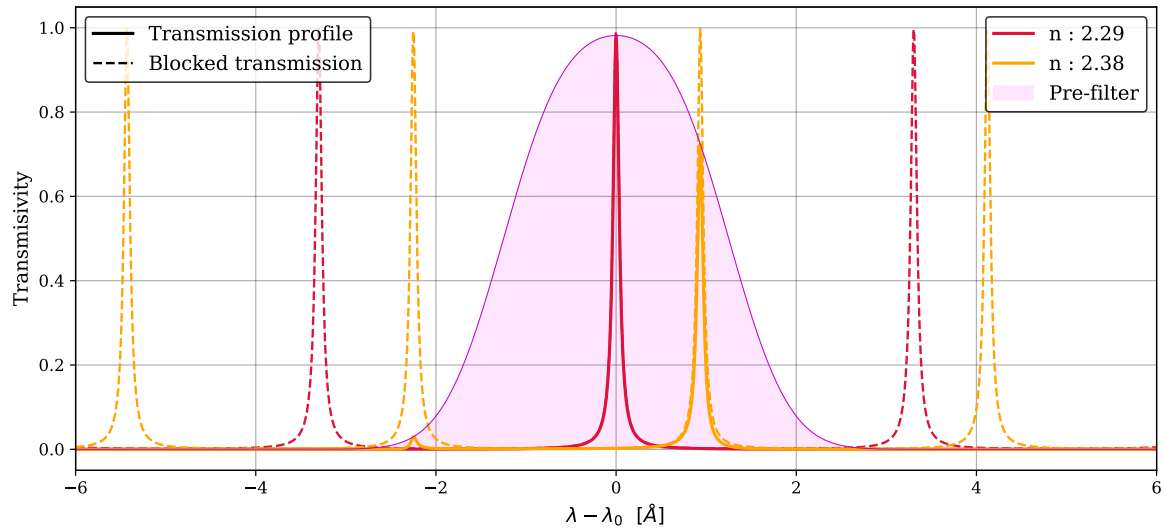


Figure 1.3 Transmission profiles of the same etalon with varying refractive indices (n). The dashed lines represent the original transmission profile, while the solid lines indicate the portion of the transmission profile that passes through the order-sorting pre-filter (shaded purple area).

maxima occurring at a wavelength  $\lambda$  such that:

**REVISAR -> VÁLIDO PARA TELECENTRIC??**

$$\lambda = \frac{2nd \cos \theta}{m}, \quad (1.12)$$

where  $n$  is the refractive index of the medium inside the cavity,  $d$  is the distance between the mirrors,  $\theta$  is the angle of incidence of the incoming light ray and  $m$  is the interferential order ( $m \in \mathbb{Z}$ ).

With Eq. (1.12) in mind, it is clear that an etalon allows for tuning the wavelengths of the transmission peaks by either changing the distance between the mirrors or by altering the refractive index. Although changing the angle of incidence also results in a wavelength shift, it introduces other issues, such as ghost images or profile broadening in telecentric configurations, among other effects. Consequently, the angle is not used for wavelength tuning.

To tune to a single wavelength (or a very narrow band around it), it is necessary to isolate one transmission peak (main order). This is typically achieved by using a pre-filter that only allows light with wavelengths near the desired measurement region to pass through. This ensures that no light reaches the etalon that could pass through it due to interference orders other than the main one (secondary orders).

Figure 1.3 shows a simulation of the spectral behavior of this optical setup. The order-sorting pre-filter is shown with a shaded purple area and the unaltered transmission profile of the etalon is shown in dashed lines for different values of the refractive index. In solid lines, the resulting transmission profile is shown, that is, the transmission allowed through

both the pre-filter and etalon at the same time.

### 1.4.3 Polarimetry

As previously noted, determining the polarization state of light requires the determination of the components of the Stokes vector. However, these parameters cannot be measured directly since we only know how to measure intensities. Since they are Thus, measuring the polarization of light always involves multiple measurements at once. Specifically, a number equal to the number of elements to be determined: four for the complete Stokes vector, or two, if only the circular polarization and total intensity are to be measured. This is the root of the difficulties in measuring polarization, as the need for multiple measurements makes them much more susceptible to spurious effects compared to individual measurements. Cambiar que es un jaleo.

Mathematically, the effect on polarization of a linear and finite system can be treated as a combination of linear transformations on the Stokes vector and, therefore, can be represented by a matrix in  $\mathbb{R}^4$ , known as the *Mueller Matrix*. Let  $\mathbf{M}$  be the matrix that describes these transformations, then the polarization state that reaches the detector follows:

$$\mathbf{I}_{out} = \mathbf{M}\mathbf{I}_{in}, \quad (1.13)$$

where  $\mathbf{I}_{in}$  and  $\mathbf{I}_{out}$  are the Stokes vectors of the light that reaches the instrument, and the detector, respectively. However, since we only know how to measure intensities, the actual quantity measured by our CCD is:

$$I_{obs} = m_{00}I_{in} + m_{01}Q_{in} + m_{02}U_{in} + m_{03}V_{in}, \quad (1.14)$$

where  $m_{0i}$  is the i-th element of the first row of the Mueller Matrix. This means that the intensity we measure is a linear combination of the different polarization states of the incoming light. To determine the values of the individual parameters  $I_{in}$ ,  $Q_{in}$ ,  $U_{in}$ , and  $V_{in}$ , further independent measurements are necessary, which can be achieved by modifying the Mueller matrix. In particular, it is easy to see that four independent measurements are required in order to construct a system of equations that allows us to determine the full Stokes vector. This process is known as modulation, and the four independent measurements are referred to as modulations.

If we denote each of the modulations by  $I_j$  with  $j \in \{1, 2, 3, 4\}$ , we can construct the following system of equations:

$$\begin{pmatrix} I_1 \\ I_2 \\ I_3 \\ I_4 \end{pmatrix} = \underbrace{\begin{pmatrix} m_{01}^1 & m_{02}^1 & m_{03}^1 & m_{04}^1 \\ m_{01}^2 & m_{02}^2 & m_{03}^2 & m_{04}^2 \\ m_{01}^3 & m_{02}^3 & m_{03}^3 & m_{04}^3 \\ m_{01}^4 & m_{02}^4 & m_{03}^4 & m_{04}^4 \end{pmatrix}}_O \begin{pmatrix} I_{in} \\ U_{in} \\ Q_{in} \\ V_{in} \end{pmatrix} \quad (1.15)$$

where the superindex in  $m_{0i}^j$  denotes the values of the Mueller Matrix for each modulation.

Through straightforward algebra, it is easy to see that the stokes vector of the incoming light can be determined by  $\mathbf{I}_{in} = \mathbf{D}\mathbf{I}_{obs}$ , where  $\mathbf{D}$  is the demodulation matrix, the inverse of the modulation matrix,  $\mathbf{O}$ , and  $\mathbf{I}_{obs}$  is the vector containing the 4 measured modulations.

Carefully determining  $\mathbf{O}$ , and consequently  $\mathbf{D}$ , during the instrument calibration process is crucial, as the accuracy of the determination of the Stokes components depends entirely upon it. It can be proven (del Toro Iniesta & Collados, 2000) that the optimum modulation scheme—the values of  $\mathbf{D}$  that enable the Stokes vector to be computed with minimal uncertainty—satisfies the conditions:

$$\varepsilon_1 \leq 1, \text{ and } \sum_{i=2}^4 \varepsilon_i^2 \leq 1, \quad (1.16)$$

where the polarimetric efficiencies for each stokes parameter ( $i = 1, 2, 3, 4$ ),  $\varepsilon_i$ , are defined as:

$$\varepsilon_i = \left( N_p \sum_{j=1}^{N_p} D_{i,j}^2 \right)^{-1/2}, \quad (1.17)$$

where  $N_p$  is the number of independent modulations. When designing the modulation scheme for a given instrument, it is essential to satisfy the efficiency conditions given in Equation (1.16) to ensure optimal polarimetric accuracy for all Stokes components. Furthermore, for equal sensitivities in the measurements of Stokes parameters Q, U, and V, the corresponding efficiencies should all be equal, with a value of  $1/\sqrt{3}$ . This is a very important result because polarimetric efficiencies are directly related to the smallest measurable polarimetric signals, the polarimetric sensitivity—essentially the inverse of the signal-to-noise ratio (SNR). This relation can be expressed as (del Toro Iniesta & Collados, 2000):

$$\left( \frac{S}{N} \right)_i = \frac{\varepsilon_i}{\varepsilon_1} \left( \frac{S}{N} \right)_1, \quad i = 2, 3, 4. \quad (1.18)$$

From equations (1.18) and (1.16) it is clear that the sensitivities for computing Stokes Q, U, and V will always be lower than that of Stokes I, as their corresponding efficiencies are smaller. To achieve an SNR of  $10^3$  in Stokes measurements, which is the sensitivity required to detect weak polarization signals, an SNR of at least  $(S/N)_0 \gtrsim 1700$  is necessary in the measurement of Stokes I for a quasi-optimal modulation scheme.

#### 1.4.4 Imaging

The high-resolution imaging that etalon-based instruments are capable of is one of the pivotal reasons for their extended use. The ability to capture a two-dimensional scene of the solar surface makes them ideal for studying solar plasma structures, which require resolutions close to 100 km on the solar surface. However, it is essential to achieve these resolutions while maintaining a sufficiently high signal-to-noise ratio to ensure the required polarimetric sensitivity.

Spectropolarimeters ultimately combine measurements in polarization, spectral, and spatial (image) domains. Consequently, the final observed intensity depends on all three properties simultaneously. By integrating the spectral behavior of the etalon and pre-filter with the polarimetric measurements, and taking into account the spatial dependence of these measurements, the observed intensity for a modulation  $j$  at any point of the focal plane  $\eta, \xi$  when the etalon is tuned at a wavelength  $\lambda_s$  is determined by:

$$I_j(\xi, \eta; \lambda_s) = g(\xi, \eta) \int_0^\infty T(\lambda) \iint O_j(\xi_0, \eta_0; \lambda) S(\xi_0, \eta_0; \xi, \eta; \lambda - \lambda_s) d\xi_0 d\eta_0 d\lambda, \quad (1.19)$$

where  $T(\lambda)$  accounts for the presence of the order-sorting pre-filter,  $S(\xi_0, \eta_0; \xi, \eta; \lambda - \lambda_s)$  accounts for the imaging response of the instrument when tuned at the wavelength  $\lambda_s$ ,  $g(\xi, \eta)$  represents a spatial gain factor that accounts for any wavelength independent pixel-to-pixel intensity fluctuations occurring in the focal plane, and  $O_j(\xi_0, \eta_0; \lambda)$  is the intensity distribution of the incoming light for a modulation  $j$  and is given by:

$$O_j(\xi_0, \eta_0; \lambda) = m_{00}^j I_{in}(\xi_0, \eta_0; \lambda) + m_{01}^j Q_{in}(\xi_0, \eta_0; \lambda) + m_{02}^j U_{in}(\xi_0, \eta_0; \lambda) + m_{03}^j V_{in}(\xi_0, \eta_0; \lambda) \quad (1.20)$$

Determining the imaging response of the instrument can be quite complex, as it is influenced not only by their physical characteristics but also by their optical configuration, whether collimated or telecentric. In Chapter 2, we provide a detailed overview of the properties of each configuration, their differences, and the challenges involved in using these devices for data correction.

Strehl ratio and Wfront error. Wilson, R. N. (2004). Reflecting Telescope Optics I: Basic Design Theory and its Historical Development. Springer. Schroeder, D. J. (2000). Astronomical Optics. Academic Press. Beckers, J. M. (1993). "Adaptive Optics for Astronomy: Principles, Performance, and Applications". Annual Review of Astronomy and Astrophysics, 31, 13-62.

SPEAK ABOUT PD.

**ADD noise Discussion?**

### 1.4.5 What do spectropolarimeters tell us about the Sun?

Spectropolarimeters are often referred to as magnetographs (e.g., TuMag), suggesting they measure magnetic fields directly. However, this is not entirely accurate. In astrophysics, the physical properties of the light source are inferred by correlating them with the observed properties of the light, rather than measuring them directly. By evaluating the polarization of sunlight at different wavelengths, spectropolarimeters enable us to infer the magnetic field and estimate plasma velocities on the solar surface.

The simplest calculation we can carry out that provides us with physical quantities of the Sun is that of the line-of-sight (LOS) velocities. Given the spectral shift of a specific absorption or emission spectral line,  $\Delta\lambda$ , with respect to its rest position,  $\lambda_0$ , the LOS

velocities can be computed with the Doppler formula:

$$v_{LOS} = \frac{\Delta\lambda}{\lambda_0} c , \quad (1.21)$$

where  $c$  stands for the speed of light in vacuum.

The polarization properties of light come into play when determining the magnetic fields. Due to Zeeman and Hanle effects, the polarity and spectroscopy of spectral lines can be altered when formed in the presence of magnetic fields. Due to the Zeeman effect, the spectral lines widen or split into different polarized components when a strong magnetic field is present (del Toro Iniesta, 2003), such as in the surroundings of sunspots and active regions. In the other hand, the Hanle effect is sensitive to weaker fields, and can be used to study the magnetic structure of solar prominences or turbulent fields in the solar photosphere (Bianda et al., 1998).

One simple strategy to employ polarization and spectral data to derive the magnetic fields is through the center-of-gravity method. According to Uitenbroek (2003), the LOS strength of the magnetic field can be obtained through:

$$B_{LOS} = \frac{\lambda_+ - \lambda_-}{2} \frac{4\pi mc}{e g_L \lambda_0^2} , \quad (1.22)$$

where  $m$  and  $e$  are the electron mass and charge respectively,  $g_L$  stands for the Landé factor and  $\lambda_+$  and  $\lambda_-$  are the centroids of the right and left circularly polarized line components, respectively, and are computed by:

$$\lambda_{\pm} = \frac{\int \lambda [I_{cont} - (I \pm V)] d\lambda}{\int [I_{cont} - (I \pm V)] d\lambda} , \quad (1.23)$$

where the subindex "*cont*" stands for the wavelength at the continuum.

The vector magnetic field (*i.e.*, strength, azimuth and inclination), and not only the LOS strength can also be derived. However, the derivation of these quantities has to be achieved through inversions of the radiative transfer equation (RTE). The applicability of the different methods to carry out this inversion is an extensive topic as there are some assumptions that can be applied in some cases but not in others, such as the weak-field or Milne-Eddington approximations, among others. For an extended discussion of this topic, we refer the interested reader to del Toro Iniesta & Ruiz Cobo (2016).



## CHAPTER 2

---

### TUMAG'S DESIGN AND CALIBRATION.

In this chapter we take the first steps of the journey of developing an instrument to observe the Sun. We will define...

Fabry-Pérot interferometers (FPIs) are widely employed in the field of solar physics. Their spectroscopic and tunability properties make them especially suitable for selecting a narrow spectral band of incoming light. They also offer a two-dimensional view of the solar scene, hence allowing for the implementation of powerful and widespread image post-processing reconstruction techniques, such as phase diversity (Gonsalves, 1982) and multi-object multi-frame blind deconvolution (MOMFBD; Van Noort et al. 2005), which are difficult to implement in slit-based spectrographs (Noda et al. 2015, van Noort 2017). Many state-of-the-art instruments use FPIs as narrowband tunable filters. Among others, these instruments include the spaceborne Polarimetric and Helioseismic Imager (Solanki et al., 2020) aboard the Solar Orbiter mission (Müller et al., 2020) (SO/PHI); the Imaging Magnetograph Experiment (IMaX) instrument (Martínez Pillet et al., 2011), which flew on the first two flights of the balloon-born SUNRISE observatory (Barthol et al. 2011, Solanki et al. 2017); and the Tunable Magnetograph (TuMag) instrument for its third edition. These instruments are based on solid LiNbO<sub>3</sub> etalons. Regarding ground-based instruments, some examples include the Crisp Imaging Spectro-Polarimeter (CRISP) at the Swedish 1-m Solar telescope (Scharmer et al., 2008) at the Observatorio del Roque de los Muchachos in La Palma, Canary Islands; the GREGOR Fabry-Perot Interferometer (GFPI; Puschmann et al. 2013, Schmidt et al. 2012) at the Observatorio del Teide in Tenerife, Canary Islands; the Visible Tunable Filter (VTF; Schmidt et al., 2016) developed for the *Daniel K. Inouye* Solar Telescope (DKIST; Rimmele et al., 2020) of the Haleakalā Observatory in Hawaii; and the future Tunable Imaging Spectropolarimeter (TIS) of the European Solar Telescope (Noda et al., 2022), all of which are based on air-gapped etalons.

The SUNRISE III mission aims to study and establish the relations and couplings between the phenomena occurring at different layers of the Sun's surface. With this purpose in mind, three different post-focal instruments were included in the design, each of them responsible of observing at different regions of the spectrum. The SUNRISE UV Spectropolarimeter and Imager (SUSI, **REFERENCIA**), which will observe the spectra between 309 nm and 417 nm; The Sunrise Chromospheric Infrared spectroPolarimeter (SCIP, **REFERENCIA**), which will observe the near-infrared; and lastly, the Tunable Magnetograph (TuMag), which will ob-

Requirements	Value
Field of view	63'' x 63''
RMS wavefront error	$W \sim \lambda/14$
Spatial sampling	3 × 3 pixels
Plate scale	0.0378'' / pixel
Polarimetric efficiencies	$\epsilon_{1,2,3} \lesssim \frac{1}{\sqrt{3}}$
SNR ratio	$(\frac{S}{N})_0 \gtrapprox 1700$
Spectral resolution	< 9 pm
Spectral lines	Fe I 5250.2 Å, Fe I 5250.6 Å and Mg I $b_2$ 5172.7 Å.
Time for a two-line observation	< 90 s

Table 2.1 Tumag scientific requirements.

serve three spectral lines in the visible, at 525.02 nm, 525.06 nm and 517 nm.

The design from scratch of an instrument such as this is very complex. There are many things that have to be meticulously designed and tested which span many fields of expertise, like optics, electronics, software, hardware, or thermal design. To avoid undue extension of this thesis, we will focus on the aspects of the design directly related to the optical properties, that is, regarding the spectral, imaging and polarimetric capabilities of the instrument.

## 2.1 Sunrise III

Sunrise III description.

## 2.2 The Tunable magnetograph: TuMag

The Tunable Magnetograph (TuMag) is a tunable imaging spectropolarimeter designed to deliver high spatial resolution images across multiple spectral lines in four distinct polarization states. Consequently, TuMag is capable of measuring the four Stokes parameters, thus enabling the inference of the three components of the magnetic field and the LOS velocities at all the selected spectral lines. Moreover, this data must be acquired following a series of strict requiremets regarding optical quality, polarimetric efficiencies, required SNR, spectral performance and time limitations. A summary of these requirements is provided in Table 2.1.

## 2.3 TuMag's design and light path.

Light is delivered to TuMag by the ISLiD system and subsequently re-imaged onto two cameras where the images are recorded. Before reaching the cameras, the light passes

through all the different subsystems of the optical unit. The first components encountered by the light are a blocking prefilter and a the filter wheels. The blocking prefilter, with a wide bandpass centered at 520 nm, is employed to eliminate unwanted spectral ranges. The filter wheels are comprised by a double-disk system (Sánchez et al., 2022) that houses the prefilters for selecting specific spectral lines and a series of calibration modules. Specifically, three prefilters are mounted on the second disk of the filter wheel, corresponding to the spectral lines Fe I 5250.2 Å, Fe I 5250.6 Å, and Mg I  $b_2$  5172.7 Å. A detailed overview of the spectral properties of these prefilters will be provided in Section XX. Additionally, the filter wheel includes a PD plate, which is used to introduce a known defocus into the final image to facilitate image reconstruction techniques, along with a linear polarizer, a plate of micropolarizers, and a pinhole set.

After passing through the filter wheels, the light is directed into the Polarization Modulation Package (PMP), a subsystem derived from the SO/PHI instrument (Álvarez-Herrero et al. 2018, Solanki et al. 2020). The PMP's primary function is to modulate the light to produce the different polarization states required to deduce the Stokes components. This is achieved using two liquid crystal variable retarders (LCVRs), which are oriented with their fast axes at 45° relative to each other. These LCVRs induce a retardance on the transmitted light that varies with the voltage applied across the crystals. The system can operate in two distinct modulation schemes: a vector modulation scheme, which generates four independent linear combinations of equally-weighted Stokes components across consecutive observations, allowing for the retrieval of the full Stokes vector after demodulation; and a longitudinal modulation scheme, which generates only two modulations, providing information solely on the intensity and circular polarization.

Following modulation, the light is directed into a LiNbO<sub>3</sub> Fabry-Pérot etalon, that likewise IMaX, is in a collimated setup and with a double pass configuration (Álvarez-Herrero et al., 2006). In this setup, after traversing the etalon once, the light is redirected by a pair of mirrors to pass through the etalon a second time. This double-pass configuration significantly enhances spectral resolution by narrowing the transmission profile. The LiNbO<sub>3</sub> etalon achieves wavelength tuning by varying the refractive index of the cavity through the application of high voltages (ranging from -4000 V to 4000 V) to the mirrors. Compared to air-gapped etalons, these kind of etalons offer the advantage of having no moving parts, which is particularly beneficial for spaceborne or balloon-borne instruments. However, this advantage comes with the need for precautions to prevent discharges caused by air ionization.

The final optical element the light encounters before reaching the cameras is a polarizing beam splitter. At this stage, the light beam is divided into two orthogonal, linearly polarized components, each directed towards a different camera. This dual-beam configuration (Lites, 1987) is designed to minimize spurious signals induced by jitter of the gondola, as it effectively cancels fluctuations from Stokes I to the other Stokes parameters that may arise due to image motion or solar evolution (*i.e.* cross-talk).

Light then reaches the cameras, where images from both are recorded and stored. After mission recovery, the data is processed on-ground to combine images from the different cameras, modulation states, and spectral lines, ultimately deriving the scientific products.

This processing and reduction of the data is accomplished using software specifically developed for TuMag, which will be extensively discussed in Section XX.

## 2.4 Instrument performance and verification.

All subsystems within the TuMag light path function collaboratively to deliver high-resolution spectroscopic data of the solar spectrum. To ensure data quality, TuMag underwent multiple verification and calibration processes, during which its spectral, polarimetric, and imaging properties were meticulously tested. These procedures, commonly referred to as end-to-end (E2E) calibration tests, were conducted at various stages of the mission. Specifically, they were performed during the assembly, integration, and verification (AIV) activities with the stand-alone instrument at INTA facilities in Madrid, Spain; during the AIV phase of the post-focus instrument (PFI) platform at MPS facilities in Göttingen, Germany; and during the TuMag AIV phase in the Sunrise III mission at ESRANGE facilities in Kiruna, Sweden. These tests were designed not only to validate the instrument’s capabilities but also to measure critical parameters such as the tuning constant of the etalon, modulation matrices, and best-focus position—each of which is vital for the optimal operation of TuMag and the subsequent data processing (see Herrero et al. (2022) for a detailed description of the tests). We will now delve into the details of the imaging, spectral and polarimetric properties of the instrument as well as the verification processes and results, as the two are intimately related.

### 2.4.1 Imaging performance.

TuMag captures photons using two custom-made cameras (Orozco Suárez et al., 2023) equipped with GPIXEL back-illuminated GSENSE400BSI detectors, each featuring a  $2k \times 2k$  pixel array, and specifically designed to meet TuMag’s scientific requirements. These cameras provide a broad FoV of  $63'' \times 63''$ , sufficient to encompass an entire medium-sized active region, with a plate scale of  $0.0378''/\text{pixel}$ .

In order to fulfill the requirement of the wavefront error of  $W \sim \lambda/14$ , the instrument must have means to correct for the additional aberrations introduced by the telescope, the image stabilization and light distribution (ISLiD) system and uncorrected jittering. For this purpose, TuMag is equipped with a PD plate in the filter wheel that allows for the assessment of PSF during the observations to apply image restoration techniques during the data processing.

The imaging E2E tests involved projecting several targets at the F4 focus, including a USAF test target, star targets, and a grid, observed both with and without the PD plate. These targets were utilized to evaluate the MTF and to assess the resolving power of TuMag. The PD measurements enabled verification of the wavefront error (WFE) derived from the MTF and an evaluation of the image quality following image restoration.

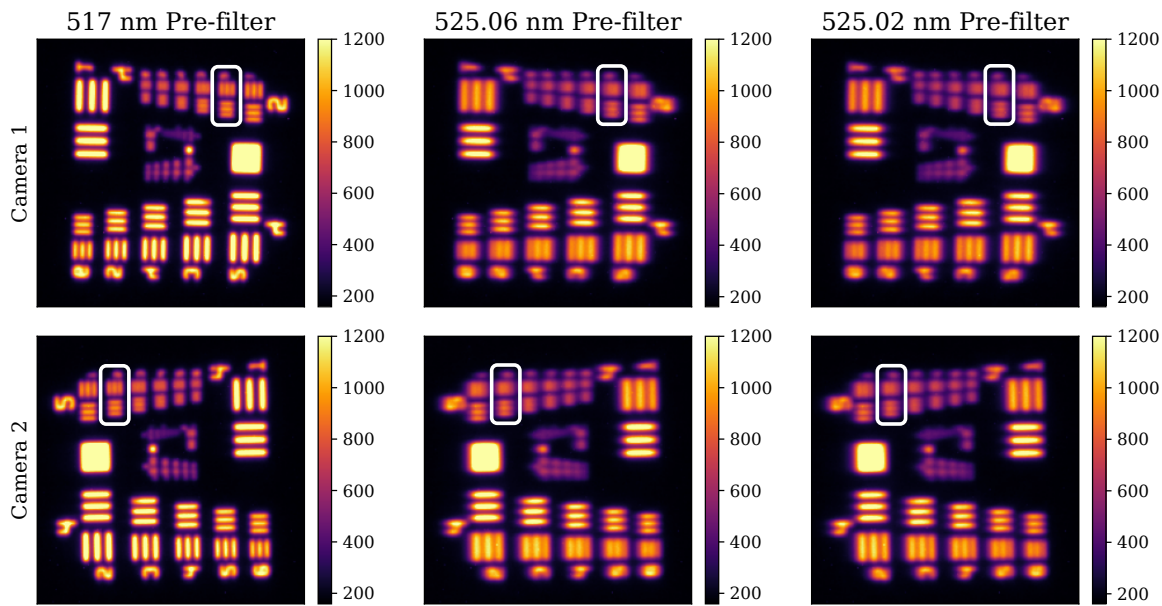


Figure 2.1 USAF target measurements for both cameras and the three pre-filters performed during E2E tests at INTA facilities on December 2021. The white boxes highlight the second element of the test group 5 (35.9 lp/mm). The scale of the images is set in digital counts.

The USAF target \* consists on a series of horizontal and vertical line pairs (lp) arranged in sets of three with varying resolutions. Identifying the highest resolution group observable with TuMag allows for a fast diagnostic of the instrument resolution and performance. In fig. 2.1, measurements of group 4 and 5 (and higher) of the USAF target are shown for both cameras and the three pre-filters. The set 2 of group 5 (highlighted in a white box), which corresponds to 35.9 lp/mm in the target and 24.3 lp/mm in the image, is of special interest since its close to the Airy disk radius (26.4 lp/mm) and therefore close to TuMag's resolution limit.

The results show a better optical performance for the 517 nm pre-filter than the other two pre-filters. The USAF 5.2 set is clearly resolved fo this pre-filter in both cameras showing almost no differene between vertical and hiorizontal resolutions. However, results for the 525 nm prefilters exhibit a worsening of the resolution, with the same set being hardly resolved in the horizontal direction in both prefilters.

However, a more precise evaluation of the optical performance can be achieved from the MTFs. Figure XX shows the MTFs computed with a slit target (see Huang et al. (2013) for a description of the MTF computation) during the E2E tests performed in December 2021 at INTA facilities. These results agree with the diagnostic carried with the USAF tests: the 517 nm pre-filter shows a good performance in both directions, with values above the expected behaviour. Meanwhile, 525 pre-filters exhibit a large difference between different directions with an important drop in vertical resolution in both cases. This observed astigmatism is attributed to the etalon and physical deformations of the pre-filters caused by

\*The 1951 USAF target from Thorlabs Inc, model: R1DS1N.

Pre-filter and camera	Strehl ratio Vertical	Strehl ratio Horizontal	WFE Vertical	WFE Horizontal
517 nm - Cam 1	0.782	0.826	$\lambda/12.7$	$\lambda/14.5$
517 nm - Cam 2	0.761	0.806	$\lambda/12.1$	$\lambda/13.5$
525.02 nm - Cam 1	0.436	0.725	$\lambda/6.9$	$\lambda/11.1$
525.02 nm - Cam 2	0.405	0.726	$\lambda/6.6$	$\lambda/11.1$
525.06 nm - Cam 1	0.451	0.764	$\lambda/7$	$\lambda/12.1$
525.06 nm - Cam 2	0.444	0.736	$\lambda/7$	$\lambda/11.3$

Table 2.2 Optical performance evaluated from the MTFs obtained with the slit target at December 2021 E2E tests.

the mechanical method used to secure and tilt them. This effect is particularly noticeable in the iron pre-filters due to the higher angles of incidence required for their tuning.

The comparison of the obtained MTF and the diffraction-limited one allows for an estimation of the Strehl ratio, and consequently the wavefront error (see section 1.4.1).

Table 2.2 shows the results for the Strehl ratios and WFE derived from this computation. All values, except for the horizontal resolution in camera 1 of the 517 nm prefilter are lower than the  $\lambda/14$  set as a requirement. However, images can always be restored if  $WFE \gtrsim \lambda/5$  (Vargas Dominguez, 2009b) if the PSF is known, thus the need for the inclusion of PD capabilities in the instrument. Furthermore, PD techniques not only allow us to enhance the optical performance of the instrument but also evaluate the optical performance during the calibrations in order to verify the results obtained through the computation of the MTF.

Figure 2.2 shows the measurements and results of the PD analysis for the 517 nm pre-filter and the camera 1. The measurements were carried out during the final E2E tests performed at Kiruna on April 2024 using the random dot target (left and central columns of the figure). The measurements consist on 5 sets of focused-defocused pairs of images. The PD algorithm is run over a zoomed-in region of 600 pixels in sub-patches of 128x128 pixels. The mean Zernike coefficients are shown in the top right panel, where the error has been computed as the standard deviation between different sub-patches. A 2D representation of the rms WFE is also shown in the bottom right panel.

The PD analysis indicates a small amplitude for most aberrations, with coefficients beyond Z15 approaching zero. Except for the spherical aberration ( $Z_{11}$ ,  $Z_4^0$ ) which is the dominant contribution to the rms wfe. However, the results exhibit significant dispersion, as reflected by error bars that reach values up to  $0.025\lambda$  for the first coefficients. Both the defocus and astigmatism are pretty low (Zernike indexes 4, 5 and 6,  $Z_2^0$ ,  $Z_2^{-2}$  and  $Z_2^2$ , respectively), agreeing with the results obtained from the MTF analysis which showed a good resolution in both vertical and horizontal directions. The overall rms WFE obtained from this analysis is  $\lambda/11.4$ . It is important to note that the PD analysis and the modulation transfer function (MTF) determination were conducted at different stages of calibration, under varying conditions, which accounts for the observed differences. Nevertheless, both analyses agree on a WFE better than  $\lambda/10$ , indicating very high optical quality, despite the fact that the FPIof TuMag operates in a collimated configuration, which is known to

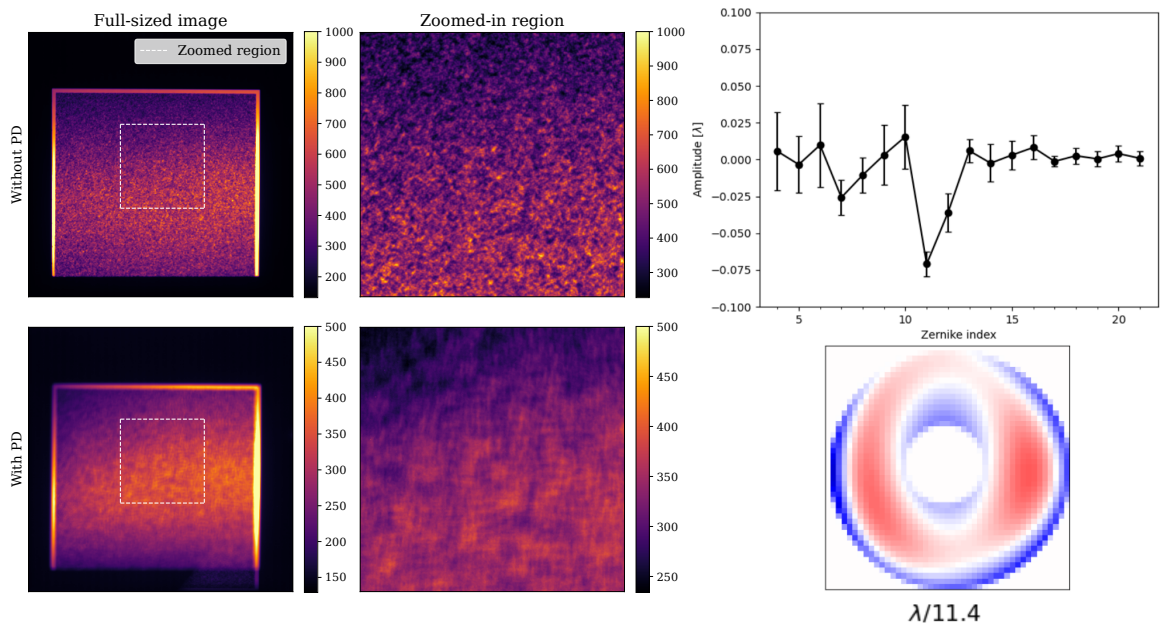


Figure 2.2 Random dot target measurements of the 517 nm pre-filter with the camera 1 and without the PD plate (left and central columns) taken during the Sunrise III AIV phase in Kiruna on April 2024. The right column shows the Zernike coefficients obtained from the PD analysis in the top panel and the 2D representation of the rms WFE. The PD analysis has been carried out by F. J. Bailén, reproduced with permission.

Property	Value
Reflectivity	0.892
Thickness	281 $\mu\text{m}$
FWHM (double-pass)	0.8
Tuning Constant	3300 V/ $\text{\AA}$

Table 2.3 Tumag Fabry-Pérot specifications.

degrade optical performance (Scharmer, 2006).

## 2.4.2 Verification

### 2.4.3 Spectral performance.

TuMag filters wavelengths through a sequential process, beginning with a broad blocking pre-filter that eliminates unwanted portions of the solar spectrum, and followed by a second narrow-band pre-filter that is tuned to the three selected spectral lines. Finally, the LiNbO<sub>3</sub> Fabry-Pérot etalon is encharged of selecting a very narrow band around specific wavelengths along the spectral lines. The narrow-band pre-filter and the etalon are critical to TuMag's spectroscopic performance and require careful evaluation during calibration.

The three TuMag pre-filters were custom-manufactured by Materion<sup>TM</sup> and have a full width at half maximum (FWHM) close to 1 nm. They are centered near the rest wavelength of the three spectral lines at normal incidence, with a peak transmission exceeding 80% in all cases. Each pre-filter was tuned by adjusting the incidence angle to align the peak transmission wavelength with the spectral line core, a process carried out using a coelostat at the INTA facilities. While this tuning was successful, particularly for the iron lines, the spectral position of the pre-filters was found to be highly sensitive to illumination conditions. This sensitivity was evident from the shifts observed in the pre-filter measurements during the various stages of the assembly process. As illustrated in the left column of Fig. 2.3, the variation in the spectral position of the pre-filters is not sufficient to cause the spectral line to be blocked by the pre-filter, but it may result in the spectral line falling on the wing of the pre-filter during observations.

TuMag's etalon (see Table 2.3) operates in a collimated setup with a transmission profile with a FWHM of 0.87 pm (in the double-passs configuration), thus achieving a spectral resolution that exceeds the required 9 pm. Observations of an iodine cell illuminated with a diode were conducted to verify the transmission profile's shape and accurately assess the tuning constant. The right column of Fig. 2.3 presents, in orange, the iodine cell measurements obtained during the assembly, integration, and verification (AIV) phase of TuMag's integration into the Post Focal Instruments (PFI) platform, which took place at the Max Planck Institute for Solar System Research (MPS) in Göttingen, Germany, in November 2023. Additionally, the dark blue line in the figure represents a simulation of the iodine spectrum observations. This simulation was generated using an analytical model of the

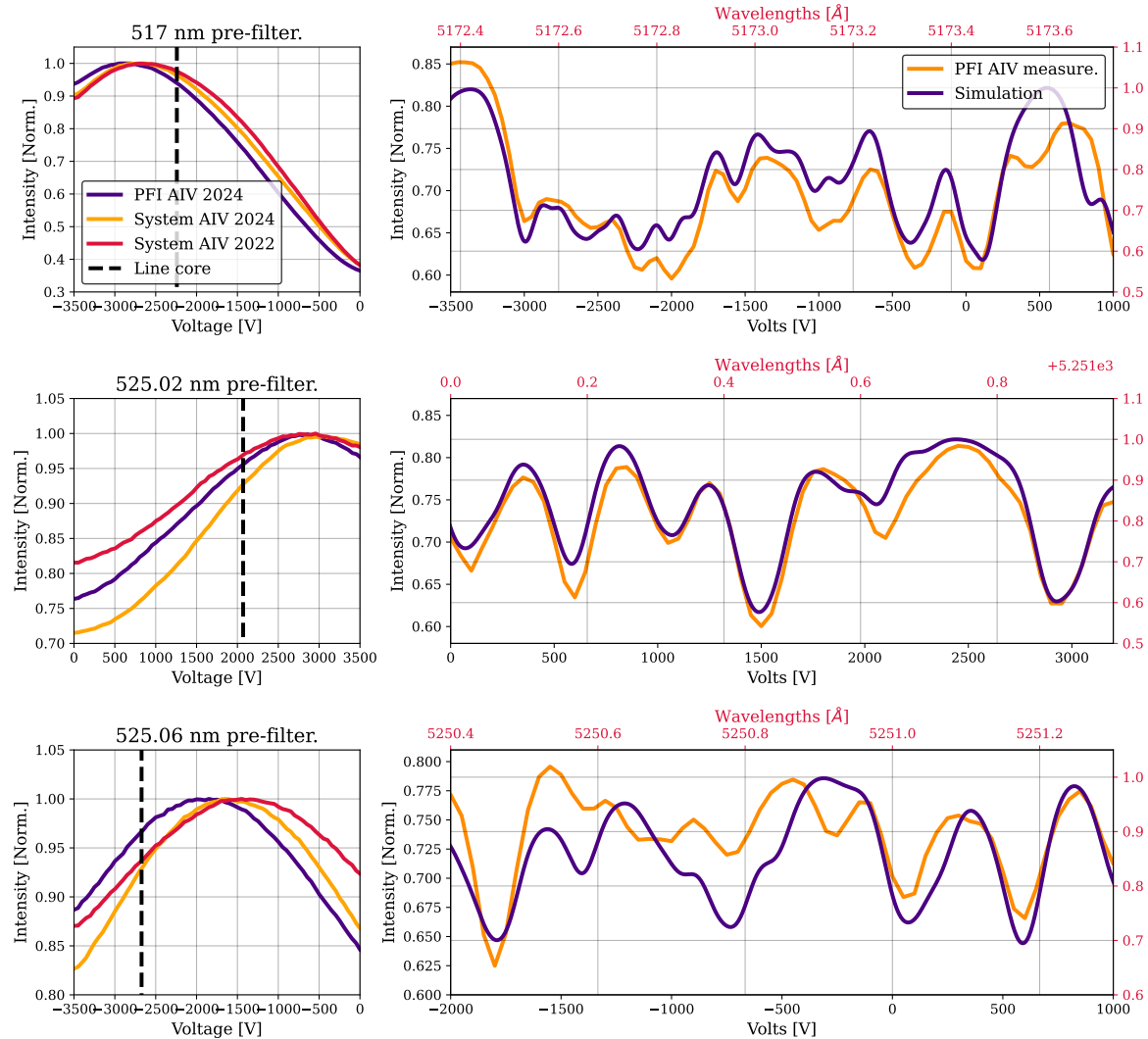


Figure 2.3 TuMag spectroscopic calibration results. Each row shows results for the 517 nm, 525.02 nm and 525.06 nm pre-filters, from top to row. The left column shows measurements of the pre-filters carried out with a flat LED on different stages of the AIV phases. The right column shows the fit of the I<sub>2</sub> cell observation with a simulation employing an etalon with a reflectivity of 0.892 (FWHM~ 0.87). Note that the absolute value of the wavelengths of the simulation (red axis) might be shifted with respect to real values due to unknown conditions of the reference.

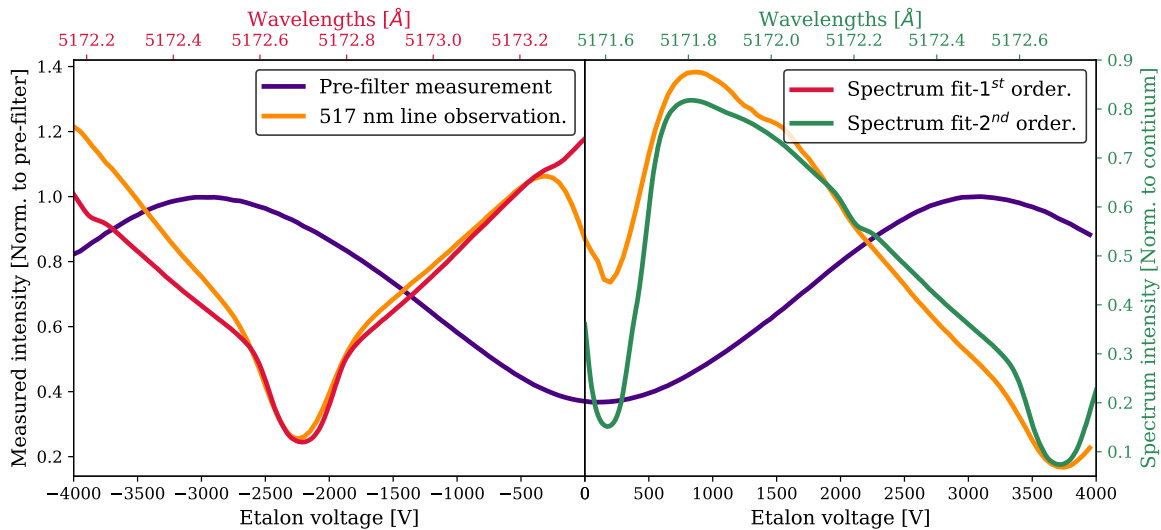


Figure 2.4 Results of the spectroscopic calibration during the end-to-end calibrations of the AIV phase of 2021. The dark blue curve represents the measurement of the 517 nm pre-filter, alongside an observation of the magnesium line using the coelostat at INTA facilities, shown in orange. Two different fits of the solar spectrum are overplotted on the figure. The red line represents a fit to the primary etalon order (negative voltages), while the green line corresponds to a fit to the second etalon order (positive voltages).

transmission profile of collimated etalons (see section ?? for a detailed overview of the model). The results confirm that the spectral resolution achieved in the iodine cell observations is consistent with the estimated 0.87 pm resolution. Furthermore, these observations enabled the calculation of the etalon's tuning constant by identifying the corresponding line cores between the simulation and observation and applying a least squares fitting to establish the relationship, which was measured in 3300 V/Å.

An observation of the solar spectrum with the 517 nm pre-filter, conducted at INTA facilities in December 2021 during the end-to-end calibration tests, is presented in Fig. 2.4, along with the corresponding pre-filter measurement. The magnesium line core is detected at approximately -2200 V using the primary order of the etalon and reappears around 3750 V with a secondary order. A fitting of the solar spectrum<sup>†</sup> is also shown for both orders. These results reveal significant contamination from the secondary order near the pre-filter's minimum transmittance. At around 0 volts, the observed spectrum (orange line) is a composite of contributions from both the primary (red line) and secondary (green line) orders. This contamination is particularly relevant for data processing, as continuum measurements of the magnesium line are typically conducted at -80 V. The broader profile of the magnesium line necessitates continuum measurements farther from the line core, making it more susceptible to this contamination. In contrast, the narrower iron lines do not require such extensive offsets for continuum measurements and are thus less affected.

---

<sup>†</sup>Reference

## CHAPTER 3

---

# TUMAG'S PIPELINE AND DATA.

INtro? tumag flew on bla vla. The data was recovered bla bla, The reduction process started on bla bla and is ongoing right now bla bla.

### 3.1 TuMag's observing modes

TuMag operates through a series of so-called observing modes. The observing modes are a list of pre-configured settings for the observations that fullfill different scientific puprposes and are meant to allow an almost automatic operation of the instrument during flight.

A summary of the properties for each observing mode is provided in Table 3.1. There are four distinct modes designed to observe the magnesium line. Mode 0s performs a fast, extended scan of the spectral line using 12 wavelength samples: [-40, -30, -20, -10, 0, 10, 20, 30, 40, 50, 60, 65]\*, with one modulation and two accumulations to maximize scanning speed. Mode 0p is similar to mode 0s but employs a full-vector modulation scheme, requiring 16 accumulations to ensure the required SNR. Mode 1 provides a shortened scan of the magnesium line, with measurements taken at [-30, -20, -10, -5, 0, 5, 10, 20, 30, 65],

\*Sampling positions are given relative to the line core.

Observing mode	Spectral lines	$N_\lambda$	$N_P$	$N_a$	$N_c$	$t_{eff}(s)$	(S/N)
0s	Mg I $b_2$ 5172.7 Å	12	1	2	1	6.3	500
0p	Mg I $b_2$ 5172.7 Å	12	4	16	1	37.62	1000
1	Mg I $b_2$ 5172.7 Å	10	4	16	1	31.81	1000
2	Fe I 5250.2 Å, Fe I 5250.6 Å	8	4	16	1	23.4	1000
3	Fe I 5250.2 Å, Fe I 5250.6 Å	5	2	20	1	10.04	1000
4	Mg I $b_2$ 5172.7 Å	3	4	10	10	54.01	2500
5	Fe I 5250.2 Å, Fe I 5250.6 Å	3	4	10	10	53.60	2500

Table 3.1 Scientific observing modes. From left to righ, the columns are: observing mode identiicator, measured spectral lines, number of wavelengths, of modulations, of accumulations, of cycles, the total timeand the polarimetric SNR.

also utilizing a vectorial modulation scheme. Finally, mode 4 is a "deep" magnetic mode, featuring a highly reduced scan with only three samples at [-10, 0, 10], but with increased accumulations and cycles to enhance polarimetric sensitivity.

Three observing modes are configured for the iron lines. Mode 2 employs a vectorial modulation scheme applicable to both iron lines, with sampling at [-12, -8, -4, 0, 4, 8, 12, 22] pm. Mode 3 uses a longitudinal modulation scheme, measuring only Stokes I and V, with samples taken at [-8, -4, 4, 8, 22] pm. Lastly, mode 5 closely resembles mode 4, but is configured for the iron lines, with sampling at [-8, 0, 8] pm. The only difference between these two modes is the sampling scheme.

### 3.1.1 Calibration modes

## 3.2 Pipeline

### 3.2.1 Darks and flat fields

### 3.2.2 Blueshift

### 3.2.3 Demodulation and dual beam

### 3.2.4 Cross Talk

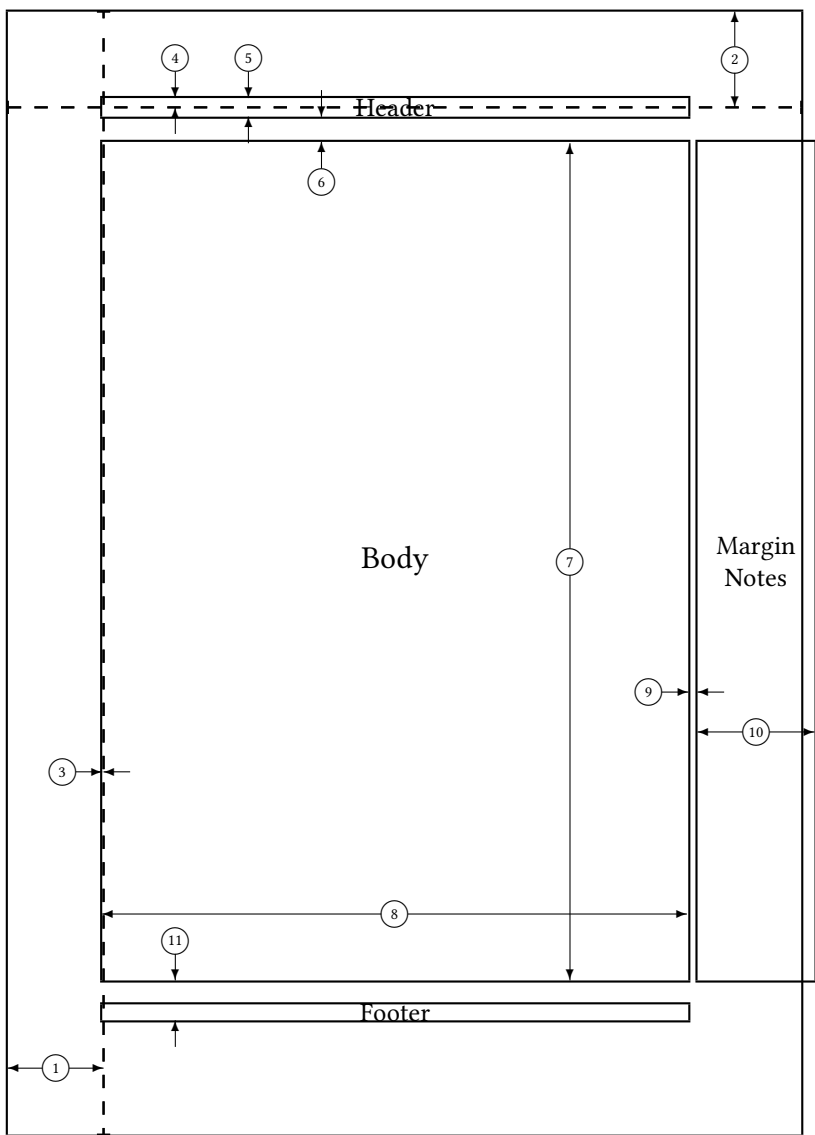
## BIBLIOGRAPHY

- Álvarez-Herrero, A., Belenguer, T., Pastor, C., et al. Lithium niobate fabry-perot etalons in double-pass configuration for spectral filtering in the visible imager magnetograph imax for the sunrise mission. *Space Telescopes and Instrumentation I: Optical, Infrared, and Millimeter*, SPIE, 797–812 (2006).
- Álvarez-Herrero, A., Parejo, P. G., & Silva-López, M. Fine tuning method for optimization of liquid crystal based polarimeters. *Optics Express* **26**, 12038 (2018).
- Bailén, F. J., Suárez, D. O., & del Toro Iniesta, J. On fabry-pérot etalon-based instruments. i. the isotropic case. *The Astrophysical Journal Supplement Series* **241**, 9 (2019).
- Barthol, P., Gandorfer, A., Solanki, S. K., et al. The sunrise mission. *Solar Physics* **268**, 1 (2011).
- Bianda, M., Solanki, S., & Stenflo, J. Hanle depolarisation in the solar chromosphere. *Astronomy and Astrophysics*, v. 331, p. 760-770 (1998) **331**, 760 (1998).
- Childlaw, R., Devaney, A., & Gonsalves, R. Analytical studies of phase estimation techniques, volume 1. *Final Technical Report* (1979).
- del Toro Iniesta, J. C. (2003), Introduction to spectropolarimetry (Cambridge university press).
- del Toro Iniesta, J. C., & Collados, M. Optimum modulation and demodulation matrices for solar polarimetry. *Applied Optics* **39**, 1637 (2000).
- del Toro Iniesta, J. C., & Ruiz Cobo, B. Inversion of the radiative transfer equation for polarized light. *Living Reviews in Solar Physics* **13**, 4 (2016).
- Gaskill, J. D. (1978), Linear systems, Fourier transforms, and optics, Vol. 56 (John Wiley & Sons).
- Gonsalves, R. A. Phase retrieval and diversity in adaptive optics. *Optical Engineering* **21**, 829 (1982).
- Herrero, A. Á., Garranzo-García, D., Núñez, A., et al. End-to-end tests of the tumag instrument for the sunrise iii mission. *Ground-based and Airborne Instrumentation for Astronomy IX*, SPIE, 791–802 (2022).

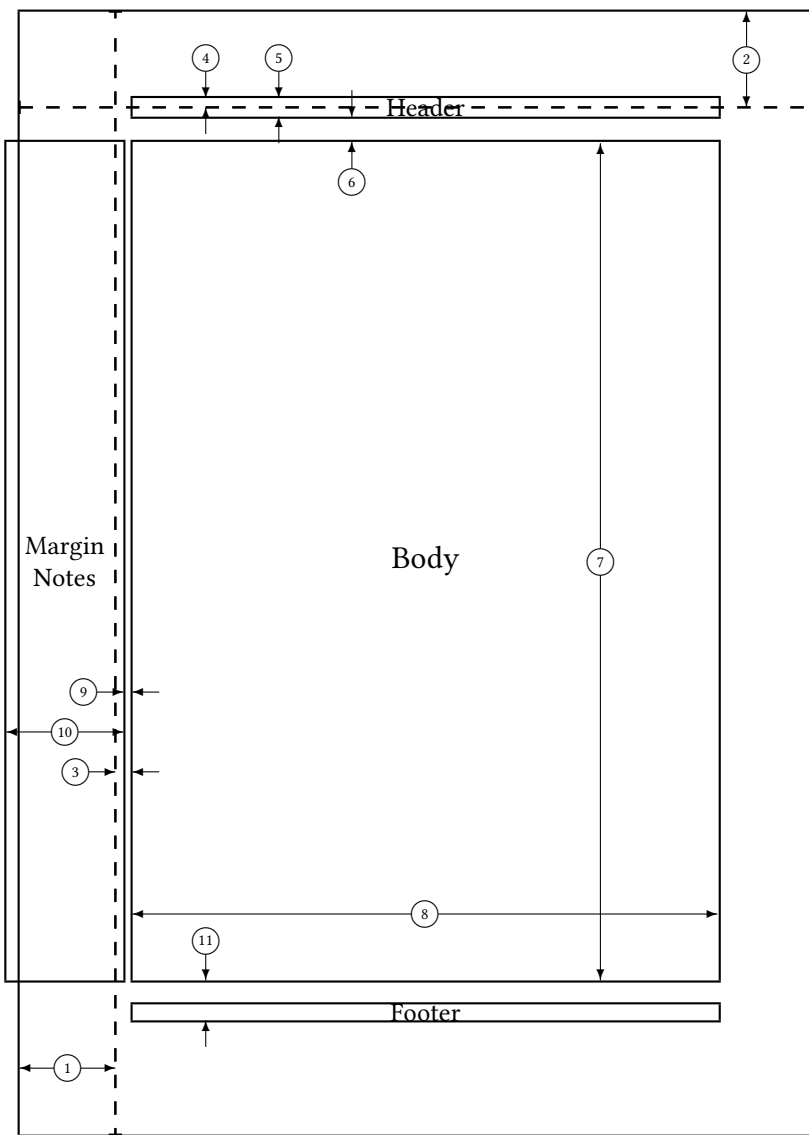
- Huang, K.-Y., Chia, C.-M., & Chang, E. Optical resolution measurement system for small lens by using slanted-slit method. *Optical Measurement Systems for Industrial Inspection VIII*, SPIE, 705–712 (2013).
- Lakshminarayanan, V., & Fleck, A. Zernike polynomials: a guide. *Journal of Modern Optics* **58**, 545 (2011).
- Lites, B. W. Rotating waveplates as polarization modulators for stokes polarimetry of the sun: evaluation of seeing-induced crosstalk errors. *Applied Optics* **26**, 3838 (1987).
- Martínez Pillet, V., Del Toro Iniesta, J., Álvarez-Herrero, A., et al. The imaging magnetograph experiment (imax) for the sunrise balloon-borne solar observatory. *Solar Physics* **268**, 57 (2011).
- Müller, D., Cyr, O. S., Zouganelis, I., et al. The solar orbiter mission-science overview. *Astronomy & Astrophysics* **642**, A1 (2020).
- Noda, C. Q., Ramos, A. A., Suárez, D. O., & Cobo, B. R. Spatial deconvolution of spectropolarimetric data: an application to quiet sun magnetic elements. *Astronomy & Astrophysics* **579**, A3 (2015).
- Noda, C. Q., Schlichenmaier, R., Rubio, L. B., et al. The european solar telescope. *Astronomy & Astrophysics* **666**, A21 (2022).
- Orozco Suárez, D., Álvarez García, D., López Jiménez, A. C., et al. Spgcam: A specifically tailored camera for solar observations. *Frontiers in Astronomy and Space Sciences* **10**, 1167540 (2023).
- Paxman, R. G., Schulz, T. J., & Fienup, J. R. Joint estimation of object and aberrations by using phase diversity. *JOSA A* **9**, 1072 (1992).
- Puschmann, K. G., Denker, C. J., Balthasar, H., et al. Gregor fabry-pérot interferometer and its companion the blue imaging solar spectrometer. *Optical Engineering* **52**, 081606 (2013).
- Rimmele, T. R., Warner, M., Keil, S. L., et al. The daniel k. inouye solar telescope—observatory overview. *Solar Physics* **295**, 1 (2020).
- Sánchez, A., Gonzalo, A., Garranzo, D., et al. High precision and thermally controlled filter wheel. *Advances in Optical and Mechanical Technologies for Telescopes and Instrumentation V*, SPIE, 1120–1135 (2022).
- Scharmer, G. Comments on the optimization of high resolution fabry-pérot filtergraphs. *Astronomy & Astrophysics* **447**, 1111 (2006).
- Scharmer, G. B., Narayan, G., Hillberg, T., et al. Crisp spectropolarimetric imaging of penumbral fine structure. *The Astrophysical Journal* **689**, L69 (2008).

- Schmidt, W., Von der Lühe, O., Volkmer, R., et al. (2012), The 1.5 meter solar telescope gregor, Wiley Online Library.
- Schmidt, W., Schubert, M., Ellwarth, M., et al. End-to-end simulations of the visible tunable filter for the daniel k. inouye solar telescope. *Ground-based and airborne instrumentation for astronomy VI*, SPIE, 1473–1483 (2016).
- Snyder, A. W. (1975), in Photoreceptor optics (Springer), 38–55.
- Solanki, S., Riethmüller, T., Barthol, P., et al. The second flight of the sunrise balloon-borne solar observatory: overview of instrument updates, the flight, the data, and first results. *The Astrophysical Journal Supplement Series* **229**, 2 (2017).
- Solanki, S. K., del Toro Iniesta, J., Woch, J., et al. The polarimetric and helioseismic imager on solar orbiter. *Astronomy & Astrophysics* **642**, A11 (2020).
- Stokes, G. G. On the composition and resolution of streams of polarized light from different sources. *Transactions of the Cambridge Philosophical Society* **9**, 399 (1851).
- Tyson, R. K. (2000), Introduction to adaptive optics, Vol. 41 (SPIE press).
- Uitenbroek, H. The accuracy of the center-of-gravity method for measuring velocity and magnetic field strength in the solar photosphere. *The Astrophysical Journal* **592**, 1225 (2003).
- van Noort, M. Image restoration of solar spectra. *Astronomy & Astrophysics* **608**, A76 (2017).
- Van Noort, M., Der Voort, L. R. V., & Löfdahl, M. G. Solar image restoration by use of multi-frame blind de-convolution with multiple objects and phase diversity. *Solar Physics* **228**, 191 (2005).
- Vargas Dominguez, S. Study of horizontal flows in solar active regions based on high-resolution image reconstruction techniques. *Ph. D. Thesis* (2009).
- Vargas Dominguez, S. Study of horizontal flows in solar active regions based on high-resolution image reconstruction techniques. *Ph. D. Thesis* (2009).
- Zernike, F. Diffraction theory of the knife-edge test and its improved form, the phase-contrast method. *Monthly Notices of the Royal Astronomical Society*, Vol. 94, p. 377-384 **94**, 377 (1934).





1 one inch + \hoffset	2 one inch + \voffset
3 \oddsidemargin = -1pt	4 \topmargin = -7pt
5 \headheight = 14pt	6 \headsep = 19pt
7 \textheight = 631pt	8 \textwidth = 441pt
9 \marginparsep = 7pt	10 \marginparwidth = 88pt
11 \footskip = 30pt \hoffset = 0pt \paperwidth = 597pt	\marginparpush = 7pt (not shown) \voffset = 0pt \paperheight = 845pt



1 one inch + \hoffset	2 one inch + \voffset
3 \evensidemargin = 13pt	4 \topmargin = -7pt
5 \headheight = 14pt	6 \headsep = 19pt
7 \textheight = 631pt	8 \textwidth = 441pt
9 \marginparsep = 7pt	10 \marginparwidth = 88pt
11 \footskip = 30pt	\marginparpush = 7pt (not shown)
\hoffset = 0pt	\voffset = 0pt
\paperwidth = 597pt	\paperheight = 845pt